

Part One
Quasiparticle Dynamics

1

Nonlinear Terahertz Studies of Ultrafast Quasiparticle Dynamics in Semiconductors

Michael Woerner and Thomas Elsaesser

Quasiparticle concepts play a fundamental role in describing the linear and nonlinear responses of semiconductors to an external electric field [1, 2]. Basic optical excitations in the range of the fundamental bandgap are the Wannier exciton and the exciton-polariton, whereas the polaron, an electron coupled to the Coulomb-mediated distortion of a polar crystal lattice, is essential for charge transport. Such quasiparticles display nonequilibrium dynamics in the femto- to picosecond time domain, governed by microscopic couplings in the electronic system and between charge carriers and lattice excitations. Ultrafast optical spectroscopy [3] in combination with extensive theoretical work [1, 4, 5] has provided detailed insight into quantum coherent quasiparticle dynamics and into a hierarchy of relaxation phenomena, including decoherence, carrier thermalization, and carrier cooling as well as trapping and recombination.

In recent years, the generation of ultrashort electric field transients in the terahertz (THz), that is, far-infrared frequency range has made substantial progress [6]. In particular, THz field strengths of up to 1 MV/cm and (sub)picosecond time structures have been achieved with the help of THz sources driven by femtosecond laser pulses. Such transients open new ways for studying charge transport in semiconductors under high-field nonequilibrium conditions [7]. Both ballistic transport phenomena, where the strong interaction of the carriers with the external field leads to negligible friction of transport on a short timescale, and the regime of coherent quantum kinetic transport become accessible. In the latter, the quantum nature of quasiparticles and their coherent quantum phase are essential, requiring a theoretical description well beyond the traditional Boltzmann equation approach based on scattering times. New phenomena occur in the time range below such scattering times, for example, quantum coherent electron-phonon interactions [8] and extended real- and k -space motions of electron wave packets.

In this chapter, we review our recent work in this exciting new area of THz research. The main emphasis is on polaron dynamics in the polar semiconductor GaAs [9] and on coherent high-field transport of electrons in the femtosecond time domain. Following this introduction, we discuss a theoretical description of the static and dynamic properties of polarons (Section 1.1.1). We then present a summary of

the experimental techniques in Section 1.1.2, followed by our results on quantum kinetic polaron dynamics (Section 1.1.3) and coherent high-field transport (Section 1.1.4). Conclusions are presented in Section 1.1.5.

1.1

Linear Optical Properties of Quasiparticles: The Polarization Cloud around a Charge Carrier

In a polar or ionic solid, a free electron distorts the crystal lattice, displacing the atoms from their equilibrium positions. One considers the electron together with its surrounding lattice distortion a quasiparticle [10, 11], the Fröhlich polaron [12, 13]. In thermal equilibrium, a Fröhlich polaron is characterized by a self-consistent attractive potential for the electron caused by a surrounding cloud of longitudinal optical (LO) phonons. In Figure 1.1, the polarized lattice (Figure 1.1a) and the potential energy as a function of the relative distance between the electron and the center of the LO phonon cloud (Figure 1.1b and c) are shown schematically. The electron-phonon coupling strength $\alpha = 0.067$ [14] determines the polaron

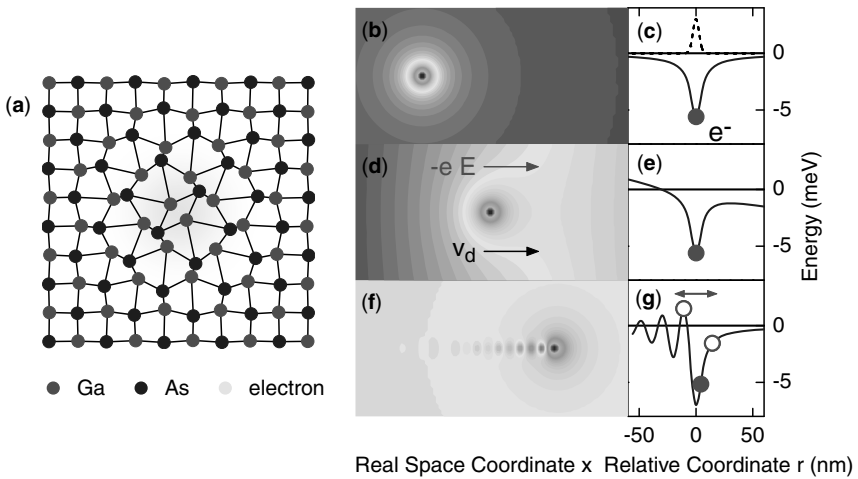


Figure 1.1 (a) Lattice distortion of the Fröhlich polaron in GaAs. Self-induced polaron potential (b, contour plot and solid line in (c)) and electron wave function (dashed line in (c)) of a polaron at rest. (d and e) Linear transport: For low applied electric fields, the total potential is the sum of the applied potential and the zero-field polaron potential. (f and g) Nonlinear transport: In a strong DC field (which has been subtracted from the potentials shown in (f) and

(g)), the drifting electron (red dot) is displaced from the minimum of the LO phonon cloud and generates coherent phonon oscillations in its stern wave. As the amplitude of coherent LO phonons exceeds a certain threshold, the polaron potential eventually causes electron oscillations (shown as open circles) along the relative coordinate r on top of the drift motion of the entire quasiparticle. (Please find a color version of this figure on the color plates.)

binding energy of 5 meV, its radius of 2.7 nm (at room temperature), and its effective mass, which is slightly larger than the effective mass of the quasifree electron.

1.1.1

Theoretical Models Describing Static and Dynamic Properties of Polarons

In this section, we first give a brief overview of the theoretical literature on polaron physics, followed by a short description of the theoretical model we used for simulations of our nonlinear THz experiments on Fröhlich polarons in n-type GaAs.

Beginning with the late 1940s, polaron physics has been the subject of extensive theoretical literature. Pioneering work was performed by Lee *et al.* [13] and by Feynman [15] who introduced the path integral method – a standard tool being applied in a wide range of theoretical studies – for describing polaron behavior. Peeters and Devreese calculated the radius, the self-induced potential, and the number of virtual optical phonons of a polaron at rest [14]. More recently, the quasistationary high-field properties were investigated. Jensen and Sauls studied polarons near the Cerenkov velocity [16] and found that strong velocity (or momentum) fluctuations on top of the drift velocity cause the strong friction force around the threshold velocity for phonon emission. Janssen and Zwerger studied the nonlinear transport of polarons [17] with the important result that “... quantum effects become irrelevant for large fields or transport velocities...” This interesting fact establishes a link to the so-called classical polaron model [18] that has much in common with the treatment by Magnus and Schoenmaker [19] who calculated “an exact solution” of the time-dependent electron velocity in the linear regime within the Caldeira–Leggett model [20]. The results of Refs [19, 21] have clearly shown that memory effects in the electron–phonon interaction or energy nonconserving transitions (or collisional broadening) lead to interferences between the electron–electric field and the electron–phonon interaction prolonging in turn the ballistic transport on ultrafast timescales.

Based on such theoretical work, we developed a new approach to get a more specific insight into the microscopic nonlinear dynamics of polarons on ultrafast timescales. We performed calculations within a nonlinear and time-dependent extension of the linear model presented in Ref. [19]. We consider a single electron interacting with the local electric field in the x -direction and with the phonon modes of the crystal via different types of electron–phonon interactions. The quantum mechanical Hamiltonian [13] reads

$$\begin{aligned}
 H(t) = & \varepsilon(\vec{p}) + exE_{\text{loc}}(t) + \sum_{b,\vec{q}} \frac{P_{b,\vec{q}}^2 + \omega_b^2(\vec{q})Q_{b,\vec{q}}^2}{2} \\
 & + \sum_{b,\vec{q}} M_b(\vec{q}) \times [P_{b,\vec{q}} \cos \vec{q}\vec{r} + \omega_b(\vec{q})Q_{b,\vec{q}} \sin \vec{q}\vec{r}],
 \end{aligned} \tag{1.1}$$

where $\vec{r} = (x, y, z)$ and $\vec{p} = (p_x, p_y, p_z)$ denote the position and momentum operators of the electron, respectively. The dispersive band structure of the lowest conduction band is described by $\varepsilon(\vec{p})$ that can be obtained from, for example, pseudopotential calculations [22–24]. For small excursions of the electron within the lowest minimum

of the conduction band, the effective mass approximation $\varepsilon(\vec{p}) = \vec{p}^2/2m_{\text{eff}}$ is sufficient to describe the polaron correctly. The local electric field $E_{\text{loc}}(t)$ is the sum of the externally applied electric field and the field re-emitted by the coherent motion of all electrons. The latter contains the linear and nonlinear responses of the system and accounts for the radiative damping of the electron motion [25]. $Q_{b,\vec{q}}$ and $P_{b,\vec{q}}$ are the coordinate and the conjugate momentum of the phonon of branch b with the wave vector $\vec{q} = (q_x, q_y, q_z)$ and angular frequency $\omega_b(\vec{q})$. For simplicity, we limit our calculations to the polar coupling to longitudinal optical phonons ($b = \text{LO}$) with a constant frequency $\omega_{\text{LO}}(\vec{q}) = \omega_{\text{LO}} = \text{const}$.

$$M_{\text{LO}}(\vec{q}) = \sqrt{\frac{e^2}{\varepsilon_0 V} \left(\frac{1}{\varepsilon_\infty} - \frac{1}{\varepsilon_S} \right)} \times \frac{1}{|\vec{q}|} \quad (1.2)$$

and coupling to acoustic phonons ($b = \text{AC}$) via the deformation potential Ξ with an averaged sound velocity c_S ,

$$M_{\text{AC}}(\vec{q}) = \sqrt{\frac{\Xi^2}{\varrho V c_S^2}}, \quad (1.3)$$

$$\omega_{\text{AC}}(\vec{q}) = \frac{2c_S q_{zb}}{\pi} \sin\left(\frac{\pi|\vec{q}|}{2q_{zb}}\right). \quad (1.4)$$

ε_S is the static relative dielectric constant and ε_∞ is the dielectric constant for frequencies well above the optical phonon frequency, but below electronic excitations. The difference $\varepsilon_\infty^{-1} - \varepsilon_S^{-1}$ is proportional to the polar electron–LO phonon coupling constant α [14]. V is the quantization volume that determines the discretization of the k - and q -spaces with the zone boundary q_{zb} and ϱ stands for the mass density of the crystal.

From Eq. (1.1), we derive the Heisenberg equations of motion for the expectation values of quantum mechanical operators like $\langle x \rangle$, $\langle p_x \rangle$, and so on. In this process, new quantum mechanical operators containing combinations of canonical variables, for example, $\langle P_{b,\vec{q}} \sin(\vec{q}\vec{r}) \rangle$, appear on the right-hand side of the equations of motion. Since we are interested only in the expectation values of the relevant observables and would like to close the infinite hierarchy of equations at some level, we expand and subsequently approximate those expectation values. In lowest order, one exactly obtains the equations of motion of the classical polaron [18, 26]. The classical polaron model predicts, however, an unrealistically high binding energy in the self-induced potential as classical particles correspond to infinitely small wave packets. To overcome this problem, one has to go one step further in the expansion of the expectation values of quantum mechanical operators and consider the finite size of the electron wave packet $\Delta x^2 = \langle x^2 \rangle - \langle x \rangle^2$. As shown in detail in Refs [27, 28], the dynamics of Δx^2 is inherently connected with the dynamics of both the variance of its conjugate momentum $\Delta p_x^2 = \langle p_x^2 \rangle - \langle p_x \rangle^2$ and $\Delta xp = \langle xp_x + p_x x \rangle / 2 - \langle x \rangle \langle p_x \rangle$, which is the covariance of x and p . The main result of Refs [27, 28] is that under certain circumstances (which are fulfilled in our case), continuous position measurements of the electron

caused by various fluctuating forces of the environment lead to decoherence phenomena in such a way that an initially Gaussian electron wave packet (in Wigner space) stays Gaussian in its further evolution and adjusts its size Δx^2 continuously to the respective momentum uncertainty according to $\Delta x^2 = \hbar^2/4\Delta p_x^2$ (cf. minimum of Heisenberg's uncertainty relation). Such continuous position measurements of the electron also lead to a small random walk in phase space, that is, diffusion of both the position and momentum of the particle. According to the arguments of the authors of Refs [27, 28], this diffusion is ineffectual in comparison to the wave packet localization and, thus, we completely neglect it in the following. The application of the approximations and arguments discussed above lead to the following system of equations of motion for the expectation values of the operators:

$$\frac{d\langle x \rangle}{dt} = \langle v_x \rangle, \quad \text{with the velocity operator } v_x = \frac{\partial \varepsilon(\vec{p})}{\partial p_x}, \quad (1.5)$$

$$\begin{aligned} \frac{d\langle p_x \rangle}{dt} = & eE_{\text{loc}}(t) + \sum_{b, \vec{q}} \exp \left[-\frac{1}{2} \vec{q}^2 \Delta x^2 \right] M_b(\vec{q}) \\ & \times [\langle P_{b, \vec{q}} \rangle q_x \sin q_x \langle x \rangle - \omega_b(\vec{q}) \langle Q_{b, \vec{q}} \rangle q_x \cos q_x \langle x \rangle], \end{aligned} \quad (1.6)$$

$$\frac{d\langle Q_{b, \vec{q}} \rangle}{dt} = \langle P_{b, \vec{q}} \rangle + M_b(\vec{q}) \cos q_x \langle x \rangle \exp \left[-\frac{1}{2} \vec{q}^2 \Delta x^2 \right], \quad (1.7)$$

$$\frac{d\langle P_{b, \vec{q}} \rangle}{dt} = -\omega_b^2(\vec{q}) \langle Q_{b, \vec{q}} \rangle - M_b(\vec{q}) \omega_b(\vec{q}) \sin q_x \langle x \rangle \exp \left[-\frac{1}{2} \vec{q}^2 \Delta x^2 \right]. \quad (1.8)$$

For simplicity, we use here spherical Gaussian wave packets with momentum $\langle p_x \rangle$ in the x -direction and isotropic momentum fluctuations $\Delta p_x^2 = \Delta p_y^2 = \Delta p_z^2$. Consequently, the expectation values of the kinetic energy $\langle \varepsilon(\vec{p}) \rangle = \varepsilon_{\text{kin}}(\langle p_x \rangle, \Delta p_x^2)$ and the velocity operator $\langle v_x \rangle = V_x(\langle p_x \rangle, \Delta p_x^2)$ are functions of both $\langle p_x \rangle$ and Δp_x^2 . Both two-dimensional functions have been derived from pseudopotential calculations [22–24]. The so far missing dynamical variable Δp_x^2 (in turn determining $\Delta x^2 = \Delta y^2 = \Delta z^2 = \hbar^2/4\Delta p_x^2$) can be inferred from an equation of motion of the kinetic energy

$$\frac{d\langle \varepsilon(\vec{p}) \rangle}{dt} = \frac{\partial \varepsilon_{\text{kin}}(\langle p_x \rangle, \Delta p_x^2)}{\partial \langle p_x \rangle} \frac{d\langle p_x \rangle}{dt} + \frac{\partial \varepsilon_{\text{kin}}(\langle p_x \rangle, \Delta p_x^2)}{\partial \Delta p_x^2} \frac{d\Delta p_x^2}{dt} \quad (1.9)$$

using the following arguments. The temporal change of the total electron energy $d\langle E(\vec{p}) \rangle/dt$ splits naturally into a ballistic coherent (first term) and an incoherent contribution (second term), the latter of which is connected to the velocity fluctuations of the electron (see also discussion of Eqs. (16) and (A4) of Ref. [16]). Since the acceleration of the electron in the external field does not change its momentum fluctuations, it exclusively contributes to the first term on the rhs of Eq. (1.9). In general, the friction force due to phonon scattering (second term rhs of Eq. (1.6)) will

contribute to both terms in Eq. (1.9). In the typical situation, however, the energy relaxation time is distinctly longer than the momentum relaxation time (cf. Figure 13 of Ref. [29]). Thus, in good approximation, we assume that the friction force exclusively contributes to the incoherent contribution of electron energy change leading to the following implicit equation of motion for the expectation value of the momentum fluctuations Δp_x^2 :

$$\begin{aligned} \frac{\partial \varepsilon_{\text{kin}}(\langle p_x \rangle, \Delta p_x^2)}{\partial \Delta p_x^2} \frac{d\Delta p_x^2}{dt} &= V_x(\langle p_x \rangle, \Delta p_x^2) \sum_{b, \vec{q}} \exp \left[-\frac{1}{2} \vec{q}^2 \Delta x^2 \right] M_b(\vec{q}) \\ &\times \left[\langle P_{b, \vec{q}} \rangle q_x \sin q_x \langle x \rangle - \omega_b(\vec{q}) \langle Q_{b, \vec{q}} \rangle q_x \cos q_x \langle x \rangle \right] \\ &+ \Gamma_{\text{loss}}(p_x, \Delta p_x^2, T_L) \\ &\times \left[\varepsilon_{\text{kin}}(\langle p_x \rangle, m_{\text{eff}} k_B T_L) - \varepsilon_{\text{kin}}(\langle p_x \rangle, \Delta p_x^2) \right]. \end{aligned} \quad (1.10)$$

Emission and absorption of incoherent phonons are described by the energy relaxation rate $\Gamma_{\text{loss}}(p_x, \Delta p_x^2, T_L)$, which is generally a “slow” process occurring on a timescale of several hundreds of femtoseconds (cf. Figure 13 of Ref. [29]). Thus, it can be well described by the Fermi’s golden rule (FGR) approach like in the semiclassical Boltzmann transport equation. In the absence of external electric fields, this term relaxes the wave packet size to its value at thermal equilibrium, that is, $\Delta p_x^2 = m_{\text{eff}} k_B T_L$.

Equations (1.5)–(1.8) are similar to those of the classical polaron [18, 26]. Quantum mechanics, that is, Planck’s constant \hbar , enters this system of equations only through the bandwidth-limited wave packet size $\Delta x^2 = \hbar^2 / 4\Delta p_x^2$, the dynamics of which is determined by Eq. (1.10). We would like to stress the fact that the corresponding dynamics of the velocity (or momentum) fluctuations is determined by incoherent heating and cooling processes, both typically occurring on a timescale of several hundreds of femtoseconds. As a consequence, one expects negligible changes of Δx^2 on ultrafast timescales < 200 fs.

Our main motivation for developing the nonlinear set of polaron equations of motion, (1.5)–(1.8) and (1.10), is their conceptual simplicity and the fact that they are tractable for arbitrary driving fields $E(t)$ on a standard personal computer. Before applying them to our nonlinear THz experiments, we calculate some linear and quasistationary properties of the polaron and compare the results with other theories and experiments.

1.1.2

Experimental Signatures of Linear and Quasistationary Polaron Properties

1.1.2.1 The Fröhlich Polaron at Rest

The radius, the self-induced potential, and the number of virtual optical phonons of a polaron at rest have been calculated by Peeters and Devreese [14]. In our model, the stationary ground state of the polaron can be simply determined by setting $\langle x \rangle$, $\langle p_x \rangle$,

and all time derivatives of Eqs. (1.5)–(1.8) and (1.10) to zero and solving the implicit equations for Δp_x^2 , $\langle Q_{b,\vec{q}} \rangle$, and $\langle P_{b,\vec{q}} \rangle$. The electric field created by the self-induced polaron potential acting on an electron at a position $\langle x \rangle \neq 0$ can be calculated with the help of the second term on the rhs of Eq. (1.6). The corresponding self-induced potential at $T_L = 300$ K is shown in Figure 1.1b and c. We find an excellent agreement with the result of the path integral method in Ref. [14].

As sketched in Figure 1.1a, the electron (yellow cloud) polarizes the surrounding lattice of cations and anions via the Coulomb interaction, resulting in turn in a self-induced potential trap for the electron (solid line in Figure 1.1c). The size and depth of this polaron potential depends self-consistently on the electron–LO phonon interaction strength α and the temperature T_L of the coupled system. In addition to the thermodynamically averaged self-induced polaron potential, the electron experiences the fluctuating Coulomb potential of the surrounding ions caused by the quantum mechanical zero-point motion and thermal fluctuations of the latter. These fluctuating forces determine the spatial extension of the electron wave packet Δx^2 (dashed line in Figure 1.1c), which is called polaron radius in Ref. [14]. With increasing lattice temperature T_L , the coherence length of the electron shrinks leading to an enhanced interaction with LO phonons of higher q vectors and concomitantly to an increased average number of virtual phonons in the polaron cloud. This extended interaction with high- q LO phonons deepens and narrows the self-induced potential trap and reduces significantly the polaron radius. As already discussed in the conclusion of Ref. [14], this leads to the counterintuitive result that the polaron binding energy, that is, the depth of the self-induced trap, increases with the temperature.

Experimentally, it is very difficult to access any of the characteristic properties of the polaron at rest. For instance, strong magnetic fields have been applied to n-type semiconductor structures to measure the cyclotron resonance frequency [30]. One expects polaronic effects once the magnetic length meets the polaron radius or once the Landau level splitting meets the LO phonon energy. The experiments of Ref. [30] have shown that a separation of polaronic signatures from other effects, for example, band structure nonparabolicity, is extremely difficult.

1.1.2.2 Frequency-Dependent Mobility of the Fröhlich Polaron

Here, we briefly reconsider the linear response as discussed in Ref. [19]. In particular, we shall show that the linear limit of our theory, that is, $|q_x \langle x \rangle| \ll 1$ for all q_x , gives the quantitatively correct frequency- and temperature-dependent mobility of the polaron $\mu(\omega, T)$, ranging from the DC mobility up to the free carrier absorption (FCA) in the mid-infrared (MIR) spectral range.

The linearized versions of Eqs. (1.5)–(1.8) are those of linearly coupled harmonic oscillators. Similar to Eq. 16 in Ref. [19], the frequency-dependent mobility $\mu(\omega)$ is obtained from an integro-differential equation, which is solved by means of the Laplace transformation:

$$\frac{d\langle v(t) \rangle}{dt} = \frac{e}{m_{\text{eff}}} E(t) - \int_{-\infty}^t dt' \alpha(t-t') \langle v(t') \rangle. \quad (1.11)$$

This equation contains the memory kernel $\alpha(t)$ that in general allows describing the influence of quantum coherences on the transport behavior, that is, quantum kinetic phenomena. For a common frequency ω_{LO} for all LO phonon modes (the interaction of the electron with acoustic phonons via the deformation potential plays a minor role in the linear regime and, thus, is neglected), one has to introduce a damping mechanism to the memory kernel $\alpha(t)$ (cf. Eq. 14 in Ref. [19]) in order to ensure an irreversible energy loss to the lattice. In contrast to the standard exponential damping, we apply here the following memory kernel:

$$\alpha(t, T) = \Omega_{\text{trap}}^2(T) \frac{\tau \cos(\omega_{\text{LO}} t)}{\tau + t}, \quad (1.12)$$

$$\Omega_{\text{trap}}^2(T) = \frac{e^2}{\epsilon_0 m_{\text{eff}} V} \left(\frac{1}{\epsilon_{\infty}} - \frac{1}{\epsilon_S} \right) \sum_{\vec{q}} \frac{q_x^2 \exp(-\vec{q}^2 \Delta x^2(T))}{|\vec{q}|^2}, \quad (1.13)$$

where $\tau = 300$ fs (for GaAs at $T = 300$ K) is the decoherence time of the memory in the electron–phonon interaction. The frequency- and temperature-dependent mobility $\mu(\omega, T)$ (solid line in Figure 1.2) calculated from Eq. (1.11) with the memory function Eq. (1.12) fits a broad range of experimental data in a quantitative way, from the DC mobility $\mu_{\text{DC}}(300 \text{ K}) \approx 9000 \text{ cm}^2/(\text{V s})$ up to the free carrier absorption in the mid-infrared spectral range: $\alpha_{\text{FCA}}(\lambda = 10 \mu\text{m}, T = 300 \text{ K}) \approx 10 \text{ cm}^{-1}$ for $N_e = 10^{17} \text{ cm}^{-3}$ [31]. The theoretical model predicts correctly the $\alpha_{\text{FCA}}(\omega, T) \propto \omega^{-3}$ dependence for mid-infrared frequencies ω above the LO phonon (cf. dotted line in Figure 1.2). The temperature dependence of both $\mu_{\text{DC}}(T)$ and $\alpha_{\text{FCA}}(\omega, T)$ is essentially determined by the temperature-dependent $\Omega_{\text{trap}}^2(T)$ (a comparison with the experiment shows that τ is almost insensitive to T).

The discussion of the linear mobility of the Fröhlich polaron in thermal equilibrium shows that the FCA in the mid-infrared spectral range is a sensitive probe of the

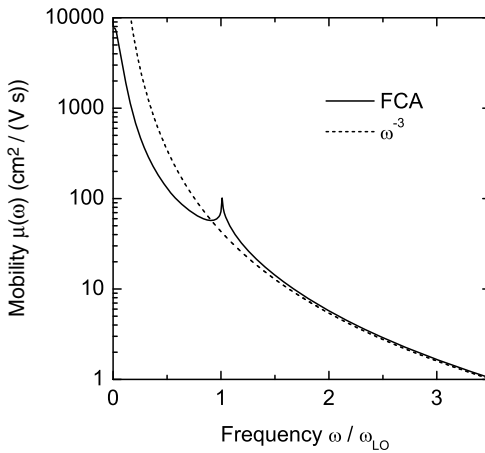


Figure 1.2 Calculated linear frequency-dependent mobility.

incoherent LO phonon population in the polaron cloud around the electron. Previously, this probe was exploited in mid-infrared pump–probe experiments on n-type InAs [32] to measure photoexcited incoherent hot, that is, nonequilibrium, phonon populations as a function of time via the transient enhancement of the free carrier absorption in the mid-infrared spectral range. So far, the theoretical description of such phenomena was based on second-order perturbation theory neglecting any coherence in the LO phonon density matrix and thus excluding possible interferences between different quantum mechanical pathways. The different theoretical approach discussed in this chapter, which is based on the quantum kinetic theory presented in Ref. [19], deals intrinsically with coherent phonons and, thus, is predetermined to describe novel FCA phenomena connected to *coherent nonequilibrium* LO phonons in the polaron cloud around the electron.

1.1.2.3 Quasistationary High-Field Transport of Polarons

In this section, we discuss the quasistationary high-field transport of polarons in GaAs. In particular, we shall show that the quasistationary drift velocity and energy of polarons are identical to results from a semiclassical Boltzmann transport equation approach. To this end, we compare the result of our polaron model with ensemble Monte Carlo simulations performed by M.V. Fischetti [29].

An external electric field E acting on the polaron (Figure 1.1d and e) induces charge transport, which is described by the drift velocity v_d . In the regime of linear response, the separation of the electron from the center of the polaron potential is negligible (Figure 1.1e) and the response to an external field is fully determined by the center-of-mass motion of the entire quasiparticle. A weak DC field (Figure 1.1d) induces a dissipative drift motion along the real space coordinate $x(t) = v_d t = \mu E t$ with a mobility $\mu = e\tau/m \approx 9000 \text{ cm}^2/(\text{V s})$ determined by the electronic charge e , the momentum relaxation time τ of the electron–phonon interaction, and the effective polaron mass m .

Above the electric field strength of $\approx 3 \text{ kV/cm}$, the drift velocity v_d starts to depend in a nonlinear way on the applied DC field E . In this regime, the quasistationary polaron potential is strongly distorted. In the frame of reference of the quasiparticle, a coherent standing wave of LO phonon oscillations appears as a stern wave of the moving electron (Figure 1.1f), similar to wake fields in plasmas [33, 34]. The enhanced generation of coherent nonequilibrium phonons in the stern wave of the quasiparticle creates the strong friction force in the nonlinear regime of polaron transport. In addition, the term with the drift velocity times the friction force in Eq. (1.10) drives the incoherent momentum fluctuations of the electron, which in turn provide access to interactions with phonons of larger q values. As a result, the wave packet size of the electron Δx^2 shrinks leading to an enhanced coupling to lattice degrees of freedom, in this way creating even higher friction forces.

The limit of quasistationary transport is achieved when we apply an electric field $E_{\text{loc}}(t)$ to Eqs. (1.5)–(1.8) and (1.10), which varies distinctly slower in time than the inverse of the incoherent energy loss rate $\Gamma_{\text{loss}}(p_x, \Delta p_x^2, T_L)$ (Eq. (1.10)) that is of the order of several hundreds of femtoseconds. The result of such a calculation is shown as symbols in Figure 1.3. In (b), we plot the drift velocity of polarons as a function of

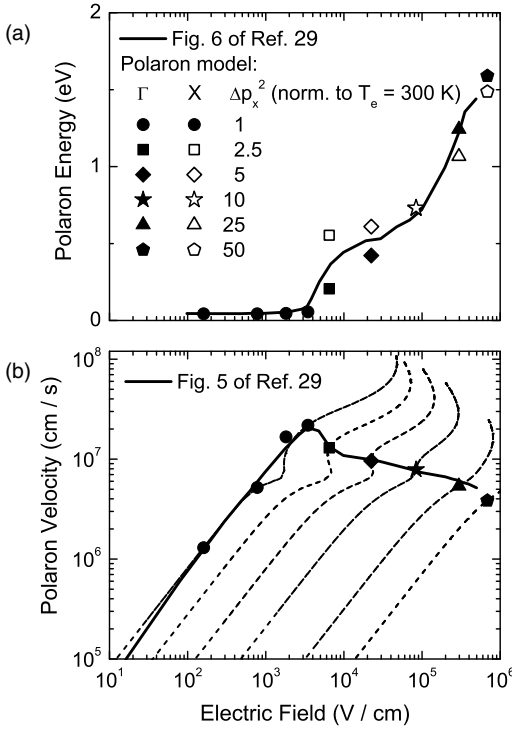


Figure 1.3 Calculated quasistationary high-field transport of polarons (symbols) in GaAs. For comparison, the black solid lines show the result of the semiclassical Boltzmann transport equation, that is, ensemble Monte Carlo simulations of M.V. Fischetti [29]. (b) Stationary drift velocity of polarons (symbols) as a function

of the applied electric field. The dashed lines show drift transport of polarons with various fixed values of the wave packet size $\Delta x^2 = \hbar^2 / 4\Delta p_x^2$. (a) Corresponding energy of the polarons in both the Γ -valley and the X-valley of the crystal.

the applied electric field strength. If the electron–phonon matrix elements (Eqs. (1.2) and (1.3)) depend exclusively on the phonon wave vector $|\vec{q}|$, one gets a common drift velocity–friction force characteristics for all electrons independent of the conduction band valley they drift in. (It is worth to mention that an additional dependence of (1.2) and (1.3) on the electron momentum \vec{p} could be easily incorporated into our model.) The dashed lines show drift transport of polarons with various *fixed* values of the wave packet size $\Delta x^2 = \hbar^2 / 4\Delta p_x^2$. Such a transport behavior is expected on a timescale, which is shorter than the respective energy relaxation time, but long enough to ensure transport in the drift limit, that is, outside the quantum kinetic regime. If this time window is large enough, one expects in this regime the well-known phenomenon of incoherent velocity overshoot, which is at the heart of the Gunn effect [35, 36]. In contrast, the polaron energy as a function of the applied field strength (Figure 1.3a) obviously depends on the electron valley. We show here the energy of the polarons in both the Γ -valley (solid symbols) and the X-valley (open symbols). The L-valley shows similar values (not shown).

Now, we compare our polaron model with the result (solid lines Figure 1.3) of the semiclassical Boltzmann transport equation calculated within the ensemble Monte Carlo approach by M.V. Fischetti [29]. The two models and experiments [37] agree excellently in the drift regime of high-field carrier transport. Thus, we have proven that our dynamic polaron model contains the results of the semiclassical Boltzmann transport equation [29] as a limiting case for a timescale on which the drift transport picture is still valid. On ultrafast timescales (i.e., $t < 300$ fs), however, the semiclassical Boltzmann transport equation fails and predicts wrong scenarios of high-field transport phenomena, as will be demonstrated in the experiments discussed in the following. In contrast, the presented polaron model, that is, Eqs. (1.5)–(1.8) and (1.10), provides correct predictions in the ultrafast time domain as well.

1.2 Femtosecond Nonlinear Terahertz and Mid-Infrared Spectroscopy

Most of the THz experiments performed so far apply THz radiation as a linear probe. Studies of the nonlinear optical response and transport require THz fields of sufficient strength. In the mid-infrared spectral range, the generation and field-resolved detection of high-field transients [38] has allowed the field-resolved nonlinear experiments on intersubband transitions in n-type modulation-doped GaAs/AlGaAs quantum wells providing valuable information on both intersubband Rabi oscillations [39–41] and nonlinear radiative coupling phenomena between quantum wells [42, 43]. Recently, we developed a simple and reliable method to generate THz pulses with high electric field amplitudes in the spectral range below 5 THz [44]. In following we first present this THz source. We then discuss nonlinear THz experiments on n-type GaAs, providing new insight into quantum kinetic transport phenomena. Such results are in sharp contrast to the predictions of the semiclassical Boltzmann transport equation [29].

1.2.1 Generation of High-Field Terahertz Transients

Despite many advances in recent years, the generation, detection, and use of electromagnetic radiation [45, 46] in the frequency range of 0.1–10 THz are still far less developed than in other frequency ranges. Most THz generation schemes [6, 47, 48] provide small electric field amplitudes in the spectral range $\nu \approx 1$ THz. The highest amplitudes (150 and 350 kV/cm) reported so far [49, 50] have been obtained using large-aperture photoconductors with bias voltages up to 45 kV. Here, we present a simple method to generate electric field amplitudes of more than 400 kV/cm. Using electro-optic sampling, we directly measure the electric field as a function of time. In this way, we fully characterize the electric fields in amplitude and phase, in contrast to interferometric methods requiring additional assumptions for field reconstruction.

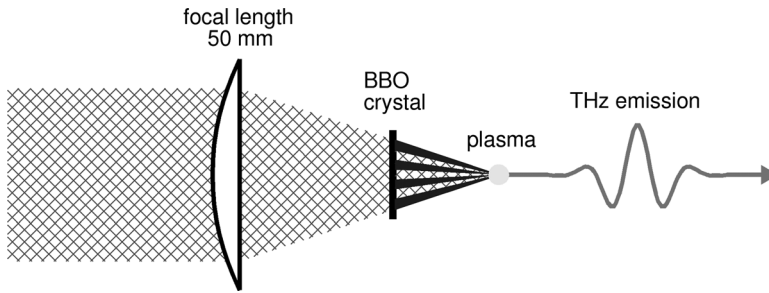


Figure 1.4 Schematic of the setup for THz generation. Incident on the lens is the output of a Ti:sapphire amplifier with pulse energies of up to 500 μ J and pulse lengths down to 25 fs. The BBO crystal of 0.1 mm thickness is cut for type-I phase-matched second-harmonic generation. In the focal region, the intensity is high enough to generate a plasma in nitrogen gas, which then acts as the source of THz radiation.

The nonlinear interaction of the fundamental (frequency ω) and the second harmonic (2ω) of femtosecond optical pulses in a laser-generated plasma in nitrogen gas is applied to generate intense THz transients. Compared to previous implementations of this method [47, 51, 52], we achieve much higher electric field amplitudes using tighter focusing and shorter pulses (both leading to higher intensities). The spectrum of the THz pulses generated extends to 7 THz, considerably higher than previously demonstrated.

Our setup for THz generation is shown schematically in Figure 1.4. A Ti:sapphire oscillator amplifier system generates pulses with a spectral width of 40 nm (corresponding to a bandwidth-limited pulse length of 22 fs) with pulse energies up to 0.5 mJ at a repetition rate of 1 kHz. Both the pulse energy and the chirp of these pulses (and thus the actual pulse length) can be varied by an acousto-optic pulse shaper [53, 54] between the oscillator and the amplifier. These pulses are focused by a fused silica lens with 50 mm focal length. A 0.1 mm thick BBO crystal cut for type-I SHG is inserted in the convergent beam about 5 mm before the focus. The THz radiation is generated in the plasma in the focal region. Both the focal length of the lens and the position of the BBO crystal are results of an optimization aimed at high electric field amplitudes. If one moves the BBO crystal closer to the focus, the intensity of the second harmonic and – as a result – the THz amplitudes become higher. This approach is, however, limited by damage in the crystal [55].

An undoped Si plate under Brewster's angle serves to separate the generated THz radiation from the remaining pump beam. Apart from its high transmission, Si has the further advantage of very low dispersion in the THz range, so it does not distort the electric field transients.

Using off-axis parabolic mirrors, the THz radiation is focused onto either a (110) ZnTe crystal or onto a (110) GaP crystal for electro-optic sampling (cf. Figure 1.7) [38]. To combine the THz radiation and the probe pulses, we use a second Si plate under Brewster's angle, which has high reflection for the s-polarized probe beam and high transmission for the p-polarized THz beam. The whole setup is enclosed and purged

with dry nitrogen gas to prevent absorption from the rotational lines of water molecules.

Electric field transients measured with a 0.4 mm thick ZnTe electro-optic crystal are shown in Figure 1.5a. The THz detection range of ZnTe is limited [56, 57] by its optical phonon resonance (5.3 THz) to frequencies below about 4 THz. To check whether the spectrum (Figure 1.5c) of the THz transient generated with the 25 fs input pulse extends to higher frequencies, we have measured the same transient with a GaP (optical phonon frequency of 11 THz) electro-optic crystal (Figure 1.5b). The latter measurement gives a much broader spectrum and an even higher amplitude of the electric field of more than 400 kV/cm, corresponding to a THz pulse energy of about 30 nJ.

Apart from providing very high electric field amplitudes, the present method of THz generation has the additional advantage of being easily tunable by changing the pulse length of the input pulse, that is, by changing the chirp with the acousto-optic pulse shaper. Transients measured with the ZnTe electro-optic crystal for different lengths of the input pulse are shown in Figure 1.5a and the corresponding spectra in Figure 1.5c.

Another interesting property of our THz plasma source is its bandwidth. A transient measured with our setup using a 0.4 mm thick ZnTe electro-optic crystal is shown in Figure 1.6a. The THz detection range of ZnTe has a gap at its optical phonon resonance around 5.3 THz. This transient was optimized for a high-frequency cutoff of the THz radiation as shown in Figure 1.6b.

1.2.2

Electric Field-Resolved THz Pump–Mid-Infrared Probe Experiments

In this section, we present the first nonlinear THz pump–mid-infrared probe experiment, which shows an interesting quantum kinetic phenomenon of the electron–LO phonon dynamics of rapidly accelerated carriers in n-type GaAs. The experimental setup is shown in Figure 1.7. Both a high-field THz transient generated by four-wave mixing in a dry nitrogen plasma [44] and a synchronized mid-infrared transient generated by difference frequency mixing in GaSe [38] are focused collinearly onto the sample, a 500 nm thick layer of Si-doped (n-type) GaAs with a carrier concentration of 10^{17} cm^{-3} (for details see Ref. [58]). After interaction with the sample, the time-dependent electric fields of the THz and MIR pulses are measured with electro-optic sampling in a thin ZnTe crystal [38]. Both the THz pump and the MIR probe beam are chopped with different frequencies allowing independent measurements of $E_{\text{THz}}(t)$, $E_{\text{MIR}}(t, \tau)$, and $E_{\text{Both}}(t, \tau)$, the latter transient with both pulses interacting with the sample. τ is the delay between the THz and the MIR pulse and t is the real time. Figure 1.8 shows such transients for $\tau = 77$ fs. The nonlinear signal of interest is obtained by subtracting the two single-color measurements from $E_{\text{Both}}(t, \tau)$: $E_{\text{NL}}(t, \tau) = E_{\text{Both}}(t, \tau) - E_{\text{THz}}(t) - E_{\text{MIR}}(t, \tau)$. The sample shows a coherent, nonlinear emission, which is for this particular τ in phase with the MIR pulse, demonstrating a THz field-induced MIR gain of the sample. The nonlinear transmission change is given by

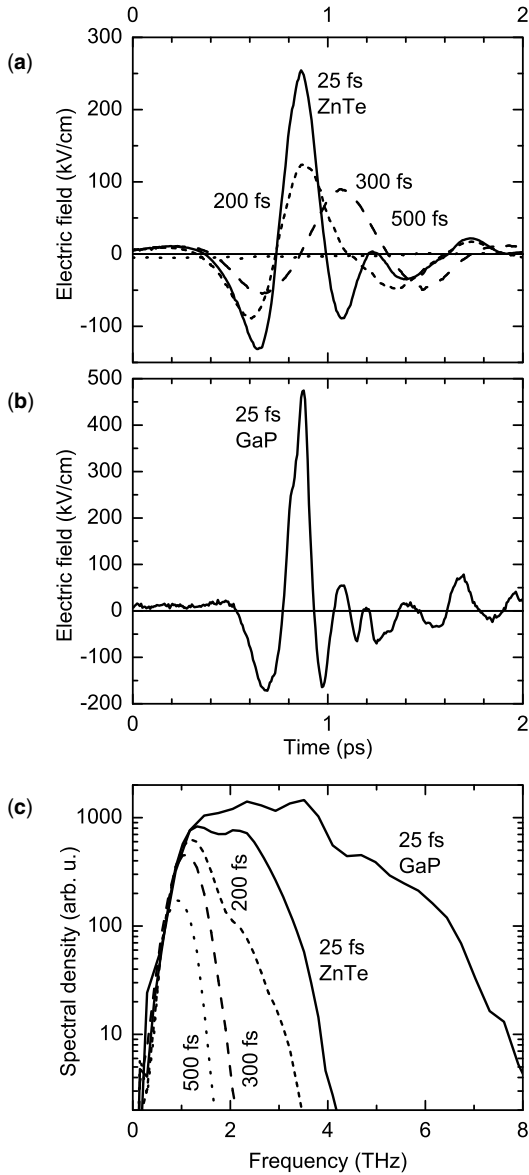


Figure 1.5 (a) Electric field transients measured by electro-optic sampling in ZnTe for different pulse lengths of the incoming pulse (pulse energy held constant at 0.5 mJ), varied by changing the amount of chirp. (b) Electric field transient for a 25 fs pulse measured by electro-

optic sampling in a 0.1 mm thick GaP crystal. (c) Spectra obtained by Fourier transform of the transients. For the shortest pulse length of 25 fs, the spectrum measured with ZnTe as electro-optic crystal shows a high-frequency cutoff around 4 THz.

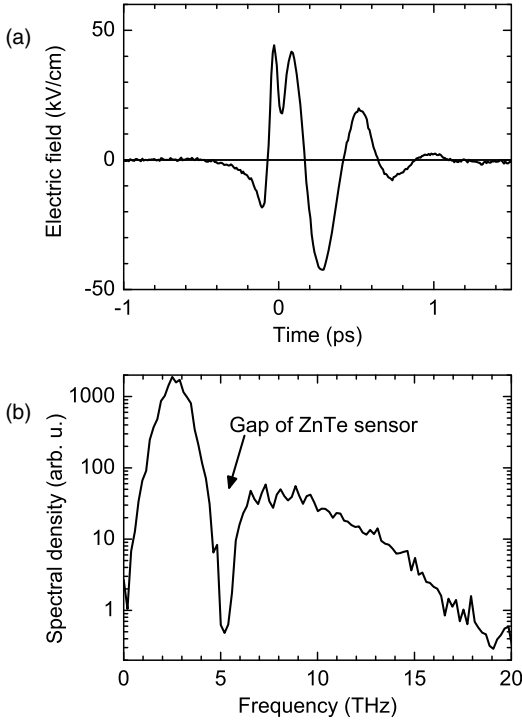


Figure 1.6 (a) Electric field transient measured by electro-optic sampling in a thin ZnTe crystal. (b) Spectrum of the pulse obtained by Fourier transform of the transient. For the shortest pump pulse length of 25 fs, we observe spectral components up to 20 THz.

$$\frac{\Delta T}{T_0}(t, \tau) = \int_{-\infty}^t E_{\text{NL}}(t', \tau) E_{\text{MIR}}(t', \tau) dt' / \int_{-\infty}^{\infty} |E_{\text{MIR}}(t', \tau)|^2 dt', \quad (1.14)$$

which is for $t \rightarrow \infty$ identical to the usual pump–probe signal.

1.2.3

Nonlinear Terahertz Transmission Experiments

In most experiments, to study the time-resolved high-field transport, one uses a static electric field [59–61]. Time resolution is obtained by photogenerating charge carriers with a short visible or near-infrared pulse. The drawbacks of this scheme are that (i) one always has electrons *and* holes, making it difficult to extract the electron response, and (ii) the possible electric field strengths are limited by electrical breakdown. To overcome such problems, we apply a strong time-dependent electric field in the THz range on n-doped GaAs, so that only electrons contribute to the transport.

The sample investigated was grown by molecular beam epitaxy and consists of a 500 nm thick freestanding layer of Si-doped (donor concentration of $N_D = 2 \times 10^{16} \text{ cm}^{-3}$) GaAs clad between two 300 nm thick $\text{Al}_{0.4}\text{Ga}_{0.6}\text{As}$ layers [62]. A few cycle

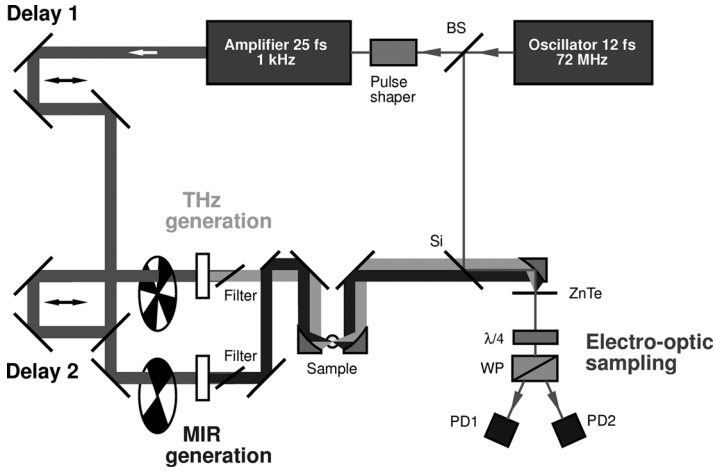


Figure 1.7 THz pump–MIR probe setup: Both terahertz $E_{\text{THz}}(t)$ and mid-infrared transients $E_{\text{MIR}}(t, \tau)$ propagate collinearly through a 500 nm thick n-type GaAs sample and are measured subsequently by electro-optic sampling in a thin ZnTe crystal. τ is the delay

between the THz and the MIR field. Dual-frequency chopping of both incoming beams allow independent measurements of E_{THz} , E_{MIR} , and E_{Both} (both pulses are transmitted through the sample).

THz pulse with a center frequency of 2 THz and a field strength in the range up to 300 kV/cm was generated by optical rectification of 25 fs pulses from a Ti:sapphire oscillator–amplifier laser system and excites the sample placed in the focus of a parabolic mirror. The direction of the electric field is along the [100] direction of the sample. With a further pair of parabolic mirrors, the electric field of the transmitted THz pulse is transferred to a thin ZnTe crystal, where it is measured via electro-optic sampling [44, 63, 64]. The optics used ensures that, apart from a sign change, the electric field transients at the sample and at the electro-optic crystal are identical (Figure 1.9a). The entire optical path of the THz beam is placed in vacuum (for experimental details, see Refs [58, 62]). The electron current density [6]

$$j(t) = -env(t) = -2E_{\text{em}}(t)/(Z_0 d) \quad (1.15)$$

in the sample is proportional to the coherently emitted field $E_{\text{em}}(t) = E_{\text{tr}}(t) - E_{\text{in}}(t)$, which is given by the difference of $E_{\text{tr}}(t)$, the field transmitted through the sample, and $E_{\text{in}}(t)$, the field incident on the sample (n is the electron density in the sample and $Z_0 = \mu_0 c = 377 \Omega$ is the impedance of free space). As the thickness of our sample $d = 500$ nm is much less than the THz wavelength $\lambda \approx 150 \mu\text{m}$, all electrons in the sample experience the same driving field, which is identical to $E_{\text{tr}}(t)$ [25, 42, 62]. It should be noted that the detection scheme applied here is different from the frequently used setup where a large area of the sample is imaged as a small focal spot on the electro-optic crystal (Figure 1.9b). In the latter case, the electric field measured at the electro-optic crystal is proportional to the time derivative of the electric field at the sample.

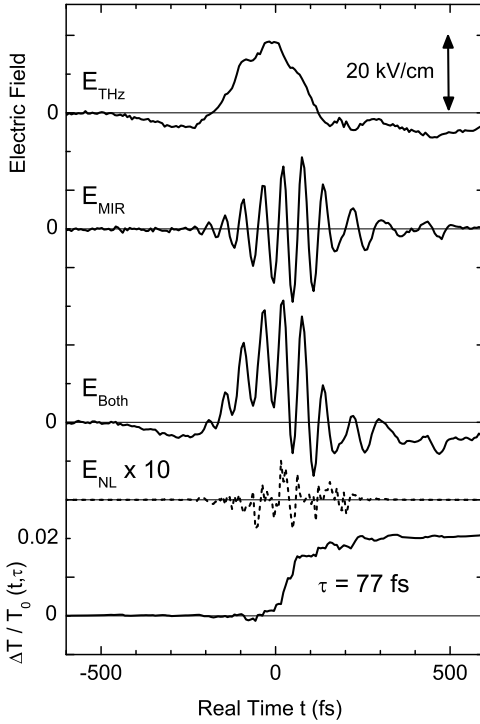


Figure 1.8 Measured transients for $\tau = 77$ fs. The curve at the bottom shows the buildup of the transmission change according to Eq. (1.14).

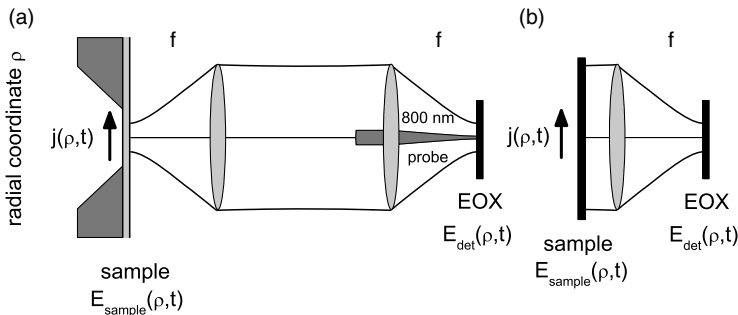


Figure 1.9 (a) Schematic of the optics used for transferring the electric field from the sample to the electro-optic crystal, EOX (in the actual setup, instead of lenses parabolic mirrors are

used). Here, the on-axis ($q = 0$) electric field at the sample is equal to minus the on-axis field at EOX, $E_{\text{sample}}(0, t) = -E_{\text{det}}(0, t)$. In contrast, in (b) $E_{\text{det}}(0, t) \propto d/dt E_{\text{sample}}(0, t)$.

1.3

Ultrafast Quantum Kinetics of Polarons in Bulk GaAs

In this section, we show that a high electric field in the terahertz range drives the polaron in a GaAs crystal into a highly nonlinear regime where – in addition to the drift motion – the electron is impulsively moved away from the center of the surrounding lattice distortion [65].

1.3.1

Experimental Results

The time-dependent electric field $E_{NL}(t, \tau)$ radiated from the nonlinear intraband polarization $E_{NL}(t, \tau) = E_{Both}(t, \tau) - E_{THz}(t) - E_{MIR}(t, \tau)$ is shown as the solid line in Figure 1.10a. The sample shows a coherent nonlinear emission, which is for this particular τ in phase with the MIR pulse, demonstrating a THz field-induced MIR gain of the sample. From $E_{NL}(t, \tau)$, we calculate the time-integrated mid-infrared transmission change $\Delta T/T_0(\tau)$ (circles in Figure 1.10b). This nonlinear signal shows an oscillatory behavior with a period of 120 fs, the period of the LO phonon in GaAs. Such oscillations correspond to a periodic switching between optical gain ($\Delta T/T_0 > 0$) and absorption ($\Delta T/T_0 < 0$) on the intraband transitions probed.

We observe the oscillatory behavior of intraband absorption and gain for THz driving fields of E_{THz} between 10 and 30 kV/cm, the maximum field applied in

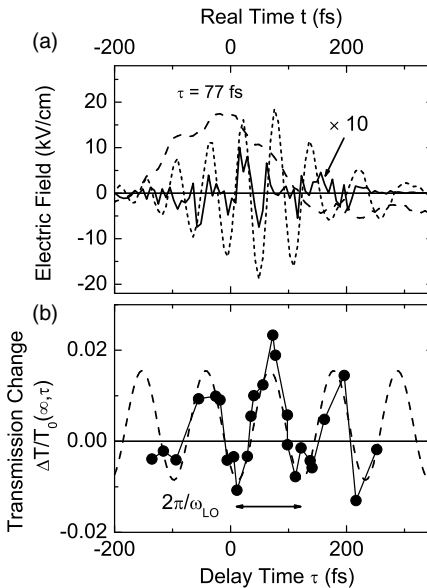


Figure 1.10 (a) $E_{THz}(t)$ (dashed line), $E_{MIR}(t, \tau)$ (dotted line), and $E_{NL}(t, \tau)$ (solid line) for $\tau = 77$ fs. (b) Transmission change $\Delta T/T_0(\infty, \tau)$ of the mid-infrared pulse as a function of τ (dots). Black dashed line: sine wave with the LO phonon frequency for comparison.

our measurements. In this range, the oscillation period does not depend on E_{THz} and is always identical to the LO phonon period. For $E_{\text{THz}} < 10$ kV/cm, oscillations are absent. Experiments with a sample of five times lower doping density do not show any nonlinear THz response. Thus, the oscillatory pump–probe signal stems exclusively from the THz excitation of electrons present by n-type doping.

The oscillatory behavior of transmission observed here for the first time is a manifestation of the highly nonlinear response of polarons to a strong external field. We analyze our findings in a nonlinear transport picture discussed in the following and described from a theoretical point in the next section. The duration of the positive half-cycle of our THz pulse (Figure 1.8) is well below the energy relaxation time of the polaron. Thus, in the drift limit, an external electric field E acting on the polaron (Figure 1.1d and e) induces charge transport, which is described by the drift velocity v_d shown as the leftmost dashed line in Figure 1.3b.

As the electron approaches the characteristic velocity of $v_0 = \sqrt{2\hbar\omega_{\text{LO}}/m} = 435$ km/s, that is, the threshold kinetic energy sufficient for emission of a LO phonon, the drift velocity v_d depends in a nonlinear way on the applied DC field E , as shown in Figures 1.3(b) (leftmost dashed line) and 1.11b and discussed in Refs [16–18, 26]. In this regime, the electron motion is described by the momentary electron velocity $v_e(t)$ and the differential mobility $\mu_{\text{diff}}(v_e) = [\partial E(v_e)/\partial v_e]^{-1}$. In our experimental scheme, we monitor such motion via the electric field $E_{\text{NL}}(t, \tau)$ (Eq. (1.14)) that is radiated from the moving charge interacting with both the driving THz field and the field $E_{\text{MIR}}(t, \tau)$ of the probe pulse. The resulting change of the mid-infrared transmission $\Delta T/T_0(\infty, \tau) \propto -(\mu_{\text{diff}}[v_e(\tau)])^{-1}$ is determined in sign and amplitude by the inverse differential mobility.

In our experiments, the polaron potential is strongly distorted by the femto-second terahertz field. First, the strong external field accelerates the electron, leading to a finite distance of the electron from the center of the polaron (along the coordinate r shown in Figure 1.1g). This distance is generated impulsively, that is, on a short timescale compared to the LO phonon oscillation period. As soon as the kinetic energy of the electron reaches $\hbar\omega_{\text{LO}}$, the electron velocity saturates by transferring energy to the lattice. Due to the impulsive character of this transfer, coherent LO phonon oscillations appear as a stern wave of the moving electron (Figure 1.1f). With increasing strength of such oscillations, the related electric field (polarization) alters the motion of the electron so that electron oscillations occur along the coordinate r with a frequency ω_{LO} (Figure 1.1g). On top of the drift motion of the entire quasiparticle with $v_{\text{polaron}}(t) \approx v_0$, the electron oscillations along the internal coordinate $r(t)$ are connected to a periodic modulation of the momentary electron velocity $v_e(t) = dr(t)/dt + v_{\text{polaron}}(t)$. In this way, the electron explores velocity regions that are characterized by different $[\mu_{\text{diff}}(v_e)]^{-1}$ of *positive* and *negative* signs (Figure 1.11b), thereby modulating the transmission of the mid-infrared probe pulses in an oscillatory manner (circles in Figure 1.10b). The oscillatory internal motion of the polaron is exposed to the fluctuating interaction with thermally excited LO phonons and influenced by other scattering mechanisms. Such processes result in a dephasing of the oscillations on

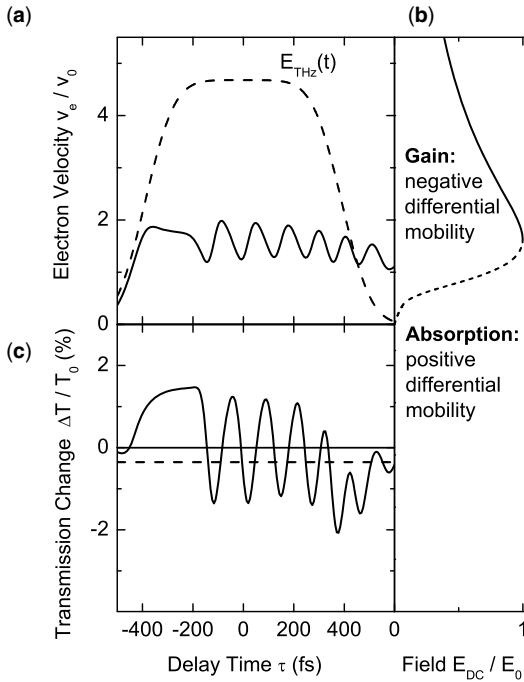


Figure 1.11 Results of model calculations. (a) Transient electron velocity (solid line) after nonlinear excitation with a strong THz field (dashed line). (b) DC drift velocity v_e as a function of the applied field E_{DC} . The transient modulation of the electron velocity in (a) and the mid-infrared transmission in (c) is caused by the periodic oscillation of v_e around the inflection point of the $v_e - E_{\text{DC}}$ characteristics changing periodically from a positive differential mobility, that is, absorption, to a negative differential mobility, that is, gain in the mid-infrared spectral range. (c) Calculated nonlinear transmission change $\Delta T / T_0(\tau)$ (solid line) of a short mid-infrared pulse as a function of τ . The transmission reduction due to linear intraband absorption is shown for comparison (dashed line).

a timescale of 0.5–1 ps, substantially longer than the time window studied in our experiments.

1.3.2

Discussion

The nonlinear response is analyzed quantitatively by considering the time-dependent self-consistent interaction potential between the electron and the LO phonon cloud already discussed in Section 1.1.1. The total local field acting on the electron is the sum of the externally applied fields [$E_{\text{THz}}(t)$ and $E_{\text{MIR}}(t, \tau)$], the field caused by the LO phonon cloud and the radiation reaction field leading to radiative damping. In Figure 1.11, the time-dependent electron velocity $v_e(\tau)$ (solid line in (a)) and the MIR transmission change (solid line in (c)) calculated for a 500 fs long terahertz pulse of 20 kV/cm amplitude (dashed line in (a)) are plotted as a function of delay time τ .

Similar to the data in Figure 1.10b, the nonlinear transmission change shows an oscillatory behavior changing periodically with the frequency of the LO phonon between gain and absorption. Even the strength of the nonlinear effect, which is approximately 10 times larger than the linear intraband absorption (dashed line in Figure 1.11c), is very well reproduced by the theory. A comparison of Figure 1.11a and c shows that – as expected and well reproduced by the theory – the oscillatory modulation of the mid-infrared transmission is directly connected to the transient motion of the electron along the internal coordinate r .

Our results highlight the quantum kinetic character of the nonlinear polaron response: the crystal lattice responds with coherent vibrations to the impulsive motion of electric charge. The timescale of such noninstantaneous process is inherently set by the LO phonon oscillation period and the picosecond decoherence of the LO phonon excitation. It is important to note that this nonlinear phenomenon occurs at comparably low electric field amplitudes of the order of $|E| = 10 \text{ kV/cm} = 0.1 \text{ V/(100 nm)}$. Thus, the quantum kinetic response plays a key role in high-frequency transport on nanometer length scales, in particular for highly polar materials such as GaN and II–VI semiconductors.

All theoretical results presented in this section were calculated on the basis of Eqs. (1.5)–(1.8) and (1.10) already discussed in Section 1.1.1. It is interesting to note that the size of the electron wave packet $\Delta x^2 = \hbar^2/4\Delta p_x^2$ remains almost constant on ultrafast timescales. There are two reasons for this behavior: (i) We start with a comparably large radius of Γ -valley polarons at room temperature, which, thanks to their high mobility, experience only a very weak friction force in the beginning. Thus, on ultrafast timescales, the first term on the rhs of Eq. (1.10) feeds the incoherent momentum fluctuations of the electron only weakly. (ii) In the quantum kinetic regime, the direction of the friction force strongly oscillates relative to that of the electron velocity leading in turn to canceling phenomena: a shrinkage and a *growth* of the wave packet size. This phenomenon is absent in the drift limit of carrier transport: here, the drift velocity and driving electric field are always in phase causing a strictly positive sign of the first term on the rhs of Eq. (1.10).

1.4

Coherent High-Field Transport in GaAs on Femtosecond Timescales

Eighty years ago, Felix Bloch showed that electron wave functions in the periodic Coulomb potential of the nuclei in a crystal are periodically modulated plane waves [66]. The spatially periodic modulation of the so-called Bloch functions restricts the allowed energies of the electrons, leading to a dispersive band structure $\varepsilon(\hbar\vec{k})$ (cf. first term on the rhs of Eq. (1.1)) containing both allowed (bands) and forbidden energy regions (gaps) [22]. Without scattering, an electron (charge $-e$) in an electric field \vec{E} is expected to follow the dispersion of its band at a constant rate in momentum space [67]

$$\hbar d\vec{k}/dt = -e\vec{E}, \quad (1.16)$$

which is identical to Eq. (1.6) without the electron–phonon interaction term. A simple integration of Eq. (1.16) reads

$$\vec{k}(t) = \vec{k}(0) - e/\hbar \int_0^t \vec{E}(t') dt'. \quad (1.17)$$

The corresponding velocity \vec{v} in real space is given by

$$\vec{v} = \hbar^{-1} \nabla_{\vec{k}} \varepsilon(\hbar\vec{k}). \quad (1.18)$$

Thus, an electron moving in the periodic Coulomb potential of a crystal under the action of a constant external electric field is expected to undergo a coherent periodic oscillation both in real and momentum space. So far, such Bloch oscillations [66] have been observed only in artificial systems such as semiconductor superlattices [68–70], atoms and/or Bose–Einstein condensates in optical lattices [71], Josephson junction arrays [72], or optical waveguide arrays [73]. The absence of Bloch oscillations in electron transport through bulk crystals has been attributed to efficient scattering of electrons on a 100 fs timescale.

In the following, we demonstrate a novel regime of electron transport in bulk crystals driven by ultrashort high-field transients in the terahertz frequency range. Electrons in bulk n-type GaAs are subject to ultrashort electric field transients with very high field amplitudes of up to 300 kV/cm. The field transmitted through the sample is measured in amplitude and phase using the techniques described in Section 1.2.3. Under such conditions, electrons at room temperature perform a coherent ballistic motion within the lowest conduction band, in this way performing a partial Bloch oscillation. The coherent current observed at a crystal temperature of 300 K agrees well with the current expected for negligible scattering. This result, which is again in strong contrast to the prediction of the semiclassical Boltzmann transport equation [29], is fully confirmed by the dynamic polaron theory based on Eqs. (1.5)–(1.8) and (1.10).

1.4.1

Experimental Results

In Figure 1.12, we present experimental results at a sample temperature of 300 K for an incident THz pulse with an amplitude of 300 kV/cm. Figure 1.12 a and b shows the transients of the incident $E_{\text{in}}(t)$ and of the transmitted $E_{\text{tr}}(t)$ pulses. The difference between these transients yields the field $E_{\text{em}}(t)$ emitted by the sample, as shown in Figure 1.12c. The velocity scale on the right-hand side is obtained from Eq. (1.15). Figure 1.12 d shows $-k(t)$ calculated according to Eq. (1.17) from $E_{\text{tr}}(t)$. $k(0)$ was taken as zero, since the electrons initially occupy the conduction band minimum near $k = 0$ (Figure 1.12e). If one now plots $v(t)$ from (c) versus $-k(t)$ from (d), one obtains the dots in (f). To clarify the connection between the curves in (c) and (d) with the dots in (f), we have marked five moments t_1 – t_5 (vertical lines in Figure 1.12a–d). Comparing these experimental results with the v versus k relationship from the conduction band structure (solid line in (f) calculated from Eq. (1.18)), one finds a good agreement, strongly pointing to ballistic transport across half the Brillouin zone.

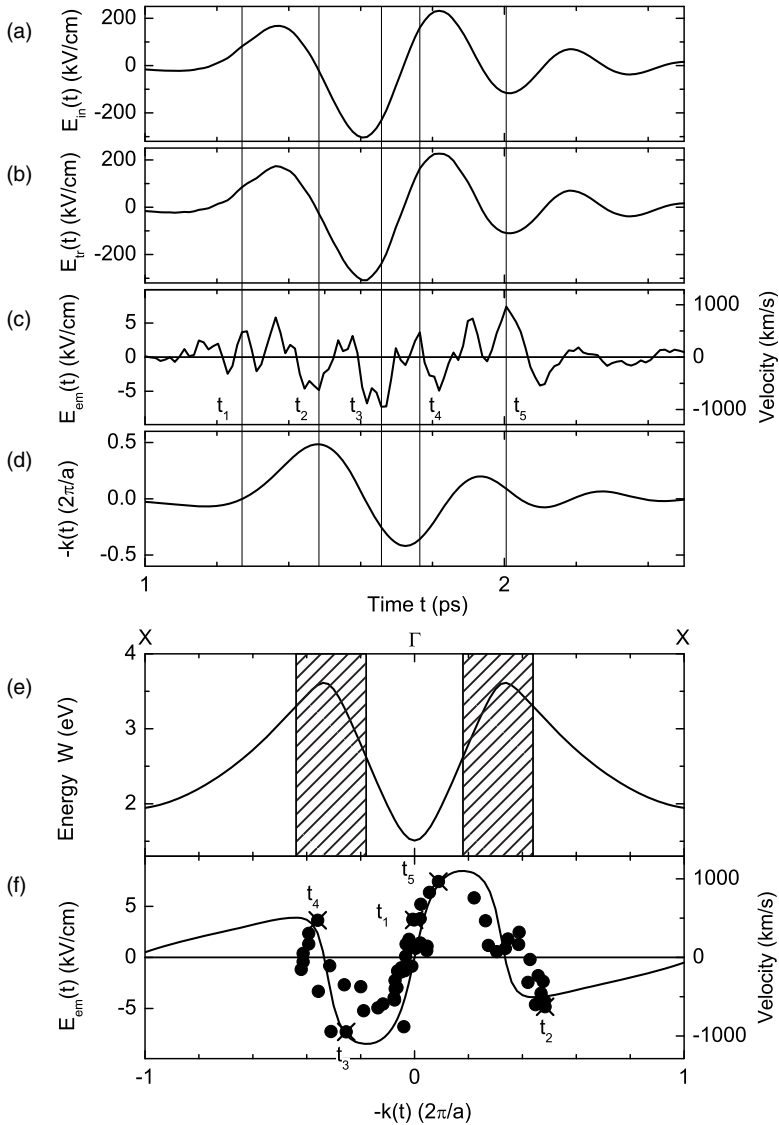


Figure 1.12 (a) Measured incident electric field as a function of time, $E_{in}(t)$. (b) Electric field transmitted through the sample, $E_{tr}(t)$. (c) Emitted electric field $E_{em}(t) = E_{tr}(t) - E_{in}(t)$. (d) $-k(t)$ calculated from the time integral of the electric field $E_{tr}(t)$ (Eq. (1.17)), in units of $2\pi/a$. (e) Lowest conduction band of GaAs in the [100]

direction. The negative mass regions are hatched. (f) Dots denote $E_{em}(t)$ plotted versus $(e/\hbar)A(t)$. Crosses show the values at the times t_1 – t_5 , marked by vertical lines in (a)–(d). (e) Solid lines denote velocity v calculated from the conduction band $\varepsilon(k)$ by $v = \hbar^{-1}d\varepsilon(\hbar k)/dk$.

To illustrate the effect of the band structure on the electron velocity, let us consider, for example, the time interval between t_2 and t_3 . During this whole time, the electric field acting on the electron is negative (Figure 1.12b). The electron velocity is negative at t_2 , then gets positive, and then gets negative again (Figure 1.12c). Thus, although the electric field has the same direction during the whole time between t_2 and t_3 , there are times with positive and times with negative acceleration. This can be reconciled with equation of motion (Newton's law) only if the effective mass of the electron changes sign, which is exactly what happens. The effective mass of a band electron is given by $m_{\text{eff}} = \hbar^2 [d^2 \epsilon(\hbar k) / dk^2]^{-1}$, that is, the sign of the effective mass is determined by the curvature of the band. In the conduction band of GaAs, the effective mass is positive around the Γ and the X points and negative around the band maxima (hatched areas in Figure 1.12e), explaining the change of the sign of the acceleration between t_2 and t_3 . One should note that even for times as late as t_5 , the data still agree with the velocity–momentum relationship expected for ballistic transport.

Our interpretation of the results is in agreement with the experimental data for all THz electric field amplitudes measured (not shown). For the two lowest applied field amplitudes (20–50 kV/cm), the emitted field $E_{\text{em}}(t)$ is approximately proportional to the time integral of the incident field, showing a linear Drude response. As we increase the field amplitude, we observe higher frequency components and a clipping of the emitted field amplitude around $|E_{\text{em}}(t)| < 7$ kV/cm. Since the emitted field is proportional to the electron velocity (Eq. (1.15)), this clipping is caused by the maximum velocity possible in the band structure. Figure 1.13 shows the emitted field (solid lines) for a particularly interesting field amplitude of 200 kV/cm of the incident field $E_{\text{in}}(t)$. At this field strength, a simulation with the traditional Boltzmann transport equation (dashed line in Figure 1.13b) completely fails, whereas our dynamic polaron model (dashed line Figure 1.13a) predicts correctly a quasiballistic high-field transport on ultrafast timescales.

1.4.2 Discussion

While our experimental results agree very well with the assumption of ballistic transport across half the Brillouin zone, the results do not agree with calculations based on the Boltzmann transport equation [29, 74]. While these calculations using Fermi's golden rule yield long scattering times (≈ 200 fs) for electrons near the conduction band minimum, the scattering times decrease markedly for electrons with an energy enabling them to scatter into side valleys (L and X). Very short times (down to 3 fs) are obtained for electrons in the negative mass regions. With such short scattering times, it would be impossible on our timescale (100 fs) to have ballistic transport across these regions. Instead, one would expect that nearly all electrons are scattered into the side valleys before reaching the negative mass regions. Since electrons in the side valleys have rather low velocities (< 200 km/s) [29, 37, 59], scattering into the side valleys would result in a drastic reduction of the electron velocity and thus of the emitted field. Since the return of electron into the Γ -valley takes quite long (> 1 ps) [75], they would remain in the side valleys for the rest of the

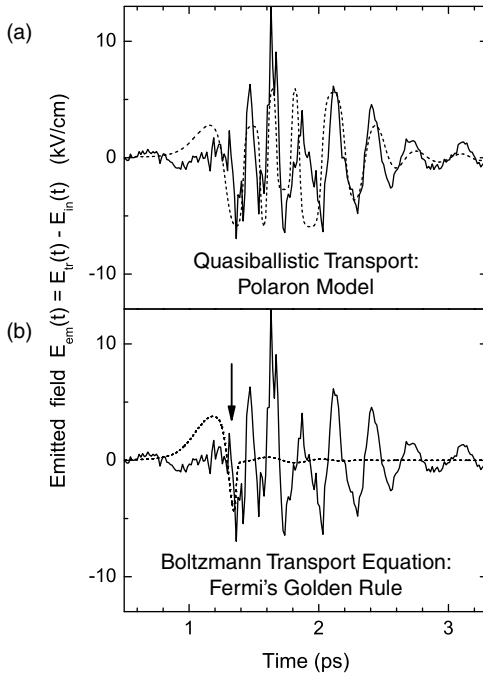


Figure 1.13 (a and b) Solid lines: emitted field transient $E_{em}(t)$ for an incident electric field $E_{in}(t)$ with an amplitude of 200 kV/cm. (a) Dashed line: result of the model calculation based on polaron model within the conduction band structure of GaAs. (b) Same experimental data as in (a), now compared to the results (dashed line) of a calculation assuming the intervalley scattering rates of Ref. [29]. At the time marked by the arrow, the electron energies are high enough for scattering into the side valleys.

pulse. Accordingly, one expects a strong signal $E_{em}(t)$ at the beginning of the pulse, but only very weak signals at later times, as shown by the dashed line in Figure 1.13b. This is in obvious disagreement with the experimental results.

To understand why calculations based on FGR do not agree with our experimental results, we have to consider the requirements for FGR to be valid. In our case, the main scattering mechanism for electrons is electron–phonon scattering, both deformation potential scattering with acoustic phonons and polar optical scattering with longitudinal optical phonons. For such periodic perturbations, FGR is only valid for times t large compared to the period of the perturbation [76], $t \gg v_{LO}^{-1} = 110$ fs [77]. Thus, FGR is not valid for the timescale of our experiment, in which the electrons are accelerated in one direction for about 250 fs. This is in contrast to most other experiments on high-field transport, which use a DC field for acceleration.

The dynamic polaron theory, which goes beyond Fermi's golden rule, predicts correctly a quasiballistic high-field transport in the quantum kinetic regime. The application of Eqs. (1.5)–(1.8) and (1.10), already discussed in Section 1.1.1, gives the result that the size of the electron wave packet $\Delta x^2 = \hbar^2/4\Delta p_x^2$ remains almost constant in our experiments on ultrafast timescales. In particular, a wave packet with

large Δx^2 couples only weakly to phonons with large wave vectors, which would allow scattering into the side valleys. Thus, on ultrafast timescales, that is, $t < 200$ fs, intervalley scattering is effectively suppressed, which yields long momentum relaxation times allowing ballistic transport over several 100 fs. On longer timescales, Δx^2 decreases.

In summary, we have observed ballistic transport of electrons in GaAs across half the Brillouin zone by time-resolved high-field THz measurements. We present a model for high-field transport using polarons that agrees quantitatively with our experimental results on short timescales and yields the drift velocity on long timescales.

1.5

Conclusions and Outlook

The results presented here demonstrate the potential of nonlinear terahertz spectroscopy to unravel transport phenomena in the highly nonlinear and quantum kinetic regime. In contrast to studies on longer timescales, the ultrashort time structure of the electric field transients allows for driving fields with amplitudes up to MV/cm. While the work presented concentrates on transport in the polar semiconductor GaAs, there is a much wider range of systems to be studied by such techniques. Beyond bulk and nanostructured semiconductors and metals, the transfer and transport of charge in inorganic and organic molecular materials is readily accessible.

The present emphasis of nonlinear terahertz studies is on understanding the basic physical processes and interactions that govern charge transport and other field-driven phenomena. With the methods of coherent pulse shaping at hand, one may go beyond such analysis and steer charge transport by interaction with phase-tailored field transients or sequences of terahertz pulses. This may lead to new concepts for electronic and optoelectronic devices.

Acknowledgments

We would like to thank our former and present coworkers P. Gaal, W. Kuehn, T. Bartel, K. Reimann, and R. Hey for their important contributions to the work reviewed here. In part, the experiments were supported by the Deutsche Forschungsgemeinschaft.

References

- 1 Haug, H. and Koch, S.W. (1993) *Quantum Theory of the Optical and Electronic Properties of Semiconductors*, World Scientific, Singapore.
- 2 Mahan, G.D. (2000) *Many-Particle Physics*, 3rd edn, Kluwer, New York.
- 3 Shah, J. (1999) *Ultrafast Spectroscopy of Semiconductors and Semiconductor Nanostructures*, 2nd edn, Springer, Berlin.
- 4 Haug, H. and Jauho, A.P. (1996) *Quantum Kinetics in Transport and Optics of Semiconductors*, Springer, Berlin.

- 5 Kuhn, T. (1998) Density matrix theory of coherent ultrafast dynamics, in *Theory of Transport Properties of Semiconductor Nanostructures* (ed. E. Schöll), Chapman & Hall, London, pp. 173–214.
- 6 Reimann, K. (2007) Table-top sources of ultrashort THz pulses. *Rep. Prog. Phys.*, **70**, 1597–1632.
- 7 Ganichev, S.D. and Prettl, W. (2006) *Intense Terahertz Excitation of Semiconductors*, Oxford University Press, Oxford.
- 8 Betz, M., Göger, G., Laubereau, A., Gartner, P., Bányai, L., Haug, H., Ortner, K., Becker, C.R., and Leitenstorfer, A. (2001) Subthreshold carrier-LO phonon dynamics in semiconductors with intermediate polaron coupling: a purely quantum kinetic relaxation channel. *Phys. Rev. Lett.*, **86**, 4684–4687.
- 9 Gaal, P., Kuehn, W., Reimann, K., Woerner, M., Elsaesser, T., and Hey, R. (2007) Internal motions of a quasiparticle governing its ultrafast nonlinear response. *Nature*, **450**, 1210–1213.
- 10 Hase, M., Kitajima, M., Constantinescu, A.M., and Petek, H. (2003) The birth of a quasiparticle in silicon observed in time–frequency space. *Nature*, **426**, 51–54.
- 11 Huber, R., Tauser, F., Brodschelm, A., Bichler, M., Abstreiter, G., and Leitenstorfer, A. (2001) How many-particle interactions develop after ultrafast excitation of an electron–hole plasma. *Nature*, **414**, 286–289.
- 12 Fröhlich, H. (1954) Electrons in lattice fields. *Adv. Phys.*, **3**, 325–361.
- 13 Lee, T.D., Low, F.E., and Pines, D. (1953) The motion of slow electrons in a polar crystal. *Phys. Rev.*, **90**, 297–302.
- 14 Peeters, F.M. and Devreese, J.T. (1985) Radius, self-induced potential, and number of virtual optical phonons of a polaron. *Phys. Rev. B*, **31**, 4890–4899.
- 15 Feynman, R.P. (1955) Slow electrons in a polar crystal. *Phys. Rev.*, **97**, 660–665.
- 16 Jensen, J.H. and Sauls, J.A. (1988) Polarons near the Cerenkov velocity. *Phys. Rev. B*, **38**, 13387–13394.
- 17 Janssen, N. and Zwerger, W. (1995) Nonlinear transport of polarons. *Phys. Rev. B*, **52**, 9406–9417.
- 18 Bányai, L. (1993) Motion of a classical polaron in a dc electric field. *Phys. Rev. Lett.*, **70**, 1674–1677.
- 19 Magnus, W. and Schoenmaker, W. (1993) Dissipative motion of an electron–phonon system in a uniform electric field: an exact solution. *Phys. Rev. B*, **47**, 1276–1281.
- 20 Caldeira, A.O. and Leggett, A.J. (1983) Path integral approach to quantum Brownian motion. *Physica*, **121**, 587–616.
- 21 Rossi, F. and Jacoboni, C. (1992) Enhancement of drift-velocity overshoot in silicon due to the intracollisional field effect. *Semicond. Sci. Technol.*, **7**, B383–B385.
- 22 Chelikowsky, J.R. and Cohen, M.L. (1976) Nonlocal pseudopotential calculations for the electronic structure of eleven diamond and zinc-blende semiconductors. *Phys. Rev. B*, **14**, 556–582: erratum, 1984, **30**, 4828.
- 23 Cohen M.L. and Bergstresser, T.K. (1966) Band structures and pseudopotential form factors for fourteen semiconductors of the diamond and zinc-blende structures. *Phys. Rev.*, **141**, 789–796.
- 24 Walter, J.P. and Cohen, M.L. (1969) Calculation of the reflectivity, modulated reflectivity, and band structure of GaAs, GaP, ZnSe, and ZnS. *Phys. Rev.*, **183**, 763–772: erratum, 1970, **B1**, 942.
- 25 Stroucken, T., Knorr, A., Thomas, P., and Koch, S.W. (1996) Coherent dynamics of radiatively coupled quantum-well excitons. *Phys. Rev. B*, **53**, 2026–2033.
- 26 Meinert, G., Bányai, L., and Gartner, P. (2001) Classical polarons in a constant electric field. *Phys. Rev. B*, **63**, 245203.
- 27 Bhattacharya, T., Habib, S., and Jacobs, K. (2002) The emergence of classical dynamics in a quantum world. *Los Alamos Sci.*, **27**, 110–125.
- 28 Bhattacharya, T., Habib, S., and Jacobs, K. (2003) Continuous quantum measurement and the quantum to classical transition. *Phys. Rev. A*, **67**, 042103.
- 29 Fischetti, M.V. (1991) Monte Carlo simulation of transport in technologically significant semiconductors of the diamond and zinc-blende structures. I. Homogeneous transport. *IEEE Trans. Electron Devices*, **38**, 634–649.

- 30 Sigg, H., Wyder, P., and Perenboom, J.A.A.J. (1985) Analysis of polaron effects in the cyclotron resonance of n-GaAs and AlGaAs-GaAs heterojunctions. *Phys. Rev. B*, **31**, 5253–5261.
- 31 Spitzer, W.G. and Whelan, J.M. (1959) Infrared absorption and electron effective mass in n-type gallium arsenide. *Phys. Rev.*, **114**, 59–63.
- 32 Elsaesser, T., Bäuerle, R.J., and Kaiser, W. (1989) Hot phonons in InAs observed via picosecond free-carrier absorption. *Phys. Rev. B*, **40**, 2976–2979.
- 33 Bingham, R. (2007) On the crest of a wake. *Nature*, **445**, 721–722.
- 34 Blumenfeld, I., Clayton, C.E., Decker, F.-J., Hogan, M.J., Huang, C., Ischebeck, R., Iverson, R., Joshi, C., Katsouleas, T., Kirby, N., Lu, W., Marsh, K.A., Mori, W.B., Muggli, P., Oz, E., Siemann, R.H., Walz, D., and Zhou, M. (2007) Energy doubling of 42 GeV electrons in a metre-scale plasma wakefield accelerator. *Nature*, **445**, 741–744.
- 35 Gunn, J.B. (1963) Microwave oscillations of current in III–V semiconductors. *Solid State Commun.*, **1**, 88–91.
- 36 Ridley, B.K. and Watkins, T.B. (1961) The possibility of negative resistance effects in semiconductors. *Proc. Phys. Soc.*, **78**, 293–304.
- 37 Windhorn, T.H., Roth, T.J., Zinkiewicz, L.M., Gaddy, O.L., and Stillman, G.E. (1982) High field temperature dependent electron drift velocities in GaAs. *Appl. Phys. Lett.*, **40**, 513–515.
- 38 Reimann, K., Smith, R.P., Weiner, A.M., Elsaesser, T., and Woerner, M. (2003) Direct field-resolved detection of terahertz transients with amplitudes of megavolts per centimeter. *Opt. Lett.*, **28**, 471–473.
- 39 Luo, C., Reimann, K., Woerner, M., and Elsaesser, T. (2004) Nonlinear terahertz spectroscopy of semiconductor nanostructures. *Appl. Phys. A*, **78**, 435–440.
- 40 Luo, C.W., Reimann, K., Woerner, M., Elsaesser, T., Hey, R., and Ploog, K.H. (2004) Phase-resolved nonlinear response of a two-dimensional electron gas under femtosecond intersubband excitation. *Phys. Rev. Lett.*, **92**, 047402–1–047404.
- 41 Luo, C.W., Reimann, K., Woerner, M., Elsaesser, T., Hey, R., and Ploog, K.H. (2004) Rabi oscillations of intersubband transitions in GaAs/AlGaAs MQWs. *Semicond. Sci. Technol.*, **19**, S285–S286.
- 42 Shih, T., Reimann, K., Woerner, M., Elsaesser, T., Waldmüller, I., Knorr, A., Hey, R., and Ploog, K.H. (2005) Nonlinear response of radiatively coupled intersubband transitions of quasi-two-dimensional electrons. *Phys. Rev. B*, **72**, 195338-1–195338-8.
- 43 Shih, T., Reimann, K., Woerner, M., Elsaesser, T., Waldmüller, I., Knorr, A., Hey, R., and Ploog, K.H. (2006) Radiative coupling of intersubband transitions in GaAs/AlGaAs multiple quantum wells. *Physica E*, **32**, 262–265.
- 44 Bartel, T., Gaal, P., Reimann, K., Woerner, M., and Elsaesser, T. (2005) Generation of single-cycle THz transients with high electric-field amplitudes. *Opt. Lett.*, **30**, 2805–2807.
- 45 Dragoman, D. and Dragoman, M. (2004) Terahertz fields and applications. *Prog. Quantum Electron.*, **28**, 1–66.
- 46 Schmuttenmaer, C.A. (2004) Exploring dynamics in the far-infrared with terahertz spectroscopy. *Chem. Rev.*, **104**, 1759–1780.
- 47 Kress, M., Löffler, T., Eden, S., Thomson, M., and Roskos, H.G. (2004) Terahertz-pulse generation by photoionization of air with laser pulses composed of both fundamental and second-harmonic waves. *Opt. Lett.*, **29**, 1120–1122.
- 48 Löffler, T., Krefß, M., Thomson, M., Hahn, T., Hasegawa, N., and Roskos, H.G. (2005) Comparative performance of terahertz emitters in amplifier-laser-based systems. *Semicond. Sci. Technol.*, **20**, S134–S141.
- 49 Budiarto, E., Margolies, J., Jeong, S., Son, J., and Bokor, J. (1996) High-intensity terahertz pulses at 1-kHz repetition rate. *IEEE J. Quantum Electron.*, **32**, 1839–1846.
- 50 You, D., Jones, R.R., Bucksbaum, P.H., and Dykaar, D.R. (1993) Generation of high-power sub-single-cycle 500-fs electromagnetic pulses. *Opt. Lett.*, **18**, 290–292.
- 51 Cook, D.J. and Hochstrasser, R.M. (2000) Intense terahertz pulses by four-wave rectification in air. *Opt. Lett.*, **25**, 1210–1212.

- 52 Hamster, H., Sullivan, A., Gordon, S., White, W., and Falcone, R.W. (1993) Subpicosecond, electromagnetic pulses from intense laser-plasma interaction. *Phys. Rev. Lett.*, **71**, 2725–2728.
- 53 Tournois, P. (1997) Acousto-optic programmable dispersive filter for adaptive compensation of group delay time dispersion in laser systems. *Opt. Commun.*, **140**, 245–249.
- 54 Verluise, F., Laude, V., Cheng, Z., Spielmann, Ch., and Tournois, P. (2000) Amplitude and phase control of ultrashort pulses by use of an acousto-optic programmable dispersive filter: pulse compression and shaping. *Opt. Lett.*, **25**, 575–577.
- 55 Allenspacher, P., Baehnisch, R., and Riede, W. (2004) Multiple ultrashort pulse damage of AR-coated beta-barium borate. *Proc. SPIE*, **5273**, 17–22.
- 56 Leitenstorfer, A., Hunsche, S., Shah, J., Nuss, M.C., and Knox, W.H. (1999) Detectors and sources for ultrabroadband electro-optic sampling: experiment and theory. *Appl. Phys. Lett.*, **74**, 1516–1518.
- 57 Wu, Q. and Zhang, X.-C. (1997) 7 terahertz broadband GaP electro-optic sensor. *Appl. Phys. Lett.*, **70**, 1784–1786.
- 58 Gaal, P., Reimann, K., Woerner, M., Elsaesser, T., Hey, R., and Ploog, K.H. (2006) Nonlinear terahertz response of n-type GaAs. *Phys. Rev. Lett.*, **96**, 187402-1–187402-4.
- 59 Abe, M., Madhavi, S., Shimada, Y., Otsuka, Y., Hirakawa, K., and Tomizawa, K. (2002) Transient carrier velocities in bulk GaAs: quantitative comparison between terahertz data and ensemble Monte Carlo calculations. *Appl. Phys. Lett.*, **81**, 679–681.
- 60 Leitenstorfer, A., Hunsche, S., Shah, J., Nuss, M.C., and Knox, W.H. (2000) Femtosecond high-field transport in compound semiconductors. *Phys. Rev. B*, **61**, 16642–16652.
- 61 Schwanhäuser, A., Betz, M., Eckardt, M., Trumm, S., Robledo, L., Malzer, S., Leitenstorfer, A., and Döhler, G.H. (2004) Ultrafast transport of electrons in GaAs: direct observation of quasiballistic motion and side valley transfer. *Phys. Rev. B*, **70**, 085211.
- 62 Gaal, P., Kuehn, W., Reimann, K., Woerner, M., Elsaesser, T., Hey, R., Lee, J.S., and Schade, U. (2008) Carrier-wave Rabi flopping on radiatively coupled shallow donor transitions in n-type GaAs. *Phys. Rev. B*, **77**, 235204-1–235204-6.
- 63 Wu, Q., Litz, M., and Zhang, X.-C. (1996) Broadband detection capability of ZnTe electro-optic field detectors. *Appl. Phys. Lett.*, **68**, 2924–2926.
- 64 Wu, Q. and Zhang, X.-C. (1995) Free-space electro-optic sampling of terahertz beams. *Appl. Phys. Lett.*, **67**, 3523–3525.
- 65 Gaal, P., Reimann, K., Woerner, M., Elsaesser, T., Hey, R., and Ploog, K.H. (2007) Nonlinear THz spectroscopy of n-type GaAs, in *Ultrafast Phenomena XV* (eds P. Corkum, D. Jonas, D. Miller, and A.M. Weiner), Springer, Berlin, pp. 799–801.
- 66 Bloch, F. (1928) Über die Quantenmechanik der Elektronen in Kristallgittern. *Z. Phys.*, **52**, 555–600.
- 67 Ridley, B.K. (1993) *Quantum Processes in Semiconductors*, 3rd edn, Oxford University Press, Oxford.
- 68 Feldmann, J., Leo, K., Shah, J., Miller, D.A.B., Cunningham, J.E., Meier, T., von Plessen, G., Schulze, A., Thomas, P., and Schmitt-Rink, S. (1992) Optical investigation of Bloch oscillations in a semiconductor superlattice. *Phys. Rev. B*, **46**, 7252–7255.
- 69 Unterrainer, K., Keay, B.J., Wanke, M.C., Allen, S.J., Leonard, D., Medeiros-Ribeiro, G., Bhattacharya, U., and Rodwell, M.J.W. (1996) Inverse Bloch oscillator: strong terahertz-photocurrent resonances at the Bloch frequency. *Phys. Rev. Lett.*, **76**, 2973–2976.
- 70 Waschke, C., Roskos, H.G., Schwedler, R., Leo, K., Kurz, H., and Köhler, K. (1993) Coherent submillimeter-wave emission from Bloch oscillations in a semiconductor superlattice. *Phys. Rev. Lett.*, **70**, 3319–3322.
- 71 Bloch, I. (2008) Quantum coherence and entanglement with ultracold atoms in optical lattices. *Nature*, **453**, 1016–1022.
- 72 Delahaye, J., Hassel, J., Lindell, R., Sillanpää, M., Paalanen, M., Seppä, H., and Hakonen, P. (2003) Low-noise current amplifier based on mesoscopic Josephson junction. *Science*, **299**, 1045–1048.

- 73 Christodoulides, D.N., Lederer, F., and Silberberg, Y. (2003) Discretizing light behaviour in linear and nonlinear waveguide lattices. *Nature*, **424**, 817–823.
- 74 Littlejohn, M.A., Hauser, J.R., and Glisson, T.H. (1977) Velocity–field characteristics of GaAs with $\Gamma_6^c - L_6^c - X_6^c$ conduction-band ordering. *J. Appl. Phys.*, **48**, 4587–4590.
- 75 Tsuruoka, T., Hashimoto, H., and Ushioda, S. (2004) Real-space observation of electron transport in AlGaAs/GaAs quantum wells using a scanning tunneling microscope. *Thin Solid Films*, **464–465**, 469–472.
- 76 Messiah, A. (1964) *Mécanique Quantique*, vol. 2, Dunod, Paris.
- 77 Holtz, M., Seon, M., Brafman, O., Manor, R., and Fekete, D. (1996) Pressure dependence of the optic phonon energies in $\text{Al}_x\text{Ga}_{1-x}\text{As}$. *Phys. Rev. B*, **54**, 8714–8720.